

Hydrothermal reworking as a mechanism forming high-grade Fe-Ti ores in layered intrusions

Dachuan Wang

Institut für Mineralogie, Leibniz Universität Hannover

Tong Hou (✉ thou@cugb.edu.cn)

State Key Laboratory of Geological Processes and Mineral Resources, China University of Geosciences, Beijing <https://orcid.org/0000-0002-8847-3018>

Roman Botchamikov

Johannes Gutenberg Universität Mainz

Stefan Weyer

Leibniz Universität Hannover

Sarah Haselbach

Institut für Mineralogie, Leibniz Universität Hannover

zhaochong Zhang

China University of Geosciences

Meng Wang

State Key Laboratory of Geological Processes and Mineral Resources, China University of Geosciences, Beijing

Ingo Horn

Institut für Mineralogie, Leibniz Universität Hannover

Francois Holtz

Leibniz Universität Hannover

Article

Keywords:

Posted Date: March 17th, 2022

DOI: <https://doi.org/10.21203/rs.3.rs-1428812/v1>

License:   This work is licensed under a Creative Commons Attribution 4.0 International License.

[Read Full License](#)

1 **Hydrothermal reworking as a mechanism forming high-grade Fe-Ti**
2 **ores in layered intrusions**

3
4 Dachuan Wang¹, Tong Hou^{2*}, Roman Botcharnikov³, Stefan Weyer¹, Sarah-Lynn
5 Haselbach¹, Zhaochong Zhang², Meng Wang², Ingo Horn¹, Francois Holtz¹

6
7 ¹ *Institut für Mineralogie, Leibniz Universität Hannover, Callinstr. 3, 30167*
8 *Hannover, Germany*

9 ² *State Key Laboratory of Geological Processes and Mineral Resources, China*
10 *University of Geosciences, Beijing 100083, China*

11 ³ *Institut für Geowissenschaften, Johannes Gutenberg Universität Mainz,*
12 *J.-J.-Becher-Weg 21, 55125 Mainz, Germany*

13

*Corresponding author. E-mail address: thou@cugb.edu.cn

14 The genesis of high-grade massive Fe-Ti oxide ores (up to >90 vol.%) in layered
15 intrusions remains highly debated. Based on *in-situ* iron isotope data ($\delta^{56}\text{Fe}$) on
16 drill-core samples from Fe-Ti oxide deposit hosted in Hongge layered intrusion, here
17 we demonstrated that hydrothermal dissolution and re-precipitation of primary
18 Fe-bearing minerals played a crucial role in the formation of the high-grade Fe-Ti
19 oxide ores. Specifically, the $\delta^{56}\text{Fe}$ data for primary magnetite (-0.23 to 0.63‰) and
20 ilmenite (-1.08 to -0.27‰) significantly exceed the typical $\delta^{56}\text{Fe}$ magmatic range.
21 Secondary magnetites formed in thick massive ore layers, display extremely low
22 $\delta^{56}\text{Fe}$ values (-1.24 to -0.09‰), indicating obvious precipitation from hydrothermal
23 fluids. Mass balance modelling suggests that about 20-30% of Fe in primary minerals
24 was hydrothermally removed and subsequently re-precipitated into the major ore
25 layers. Such hydrothermal reworking is expected to significantly increase both ore
26 tonnages and grades of the Fe-Ti oxide ores.

27

28 Layered intrusions are large sill-like igneous bodies, which exhibit compositional,
29 mineralogical and textural layering as a result of magma differentiation processes.
30 Iron (Fe) ores, often hosted in layered intrusions¹⁻⁵ are one of the major sources for Fe,
31 Ti (titanium) and V (vanadium) metals used in industry. However, the formation of
32 thick massive Fe-Ti oxide layers (usually tens meters thick) in these intrusions is still
33 under debate and several genetic models have been invoked, predominantly involving
34 magmatic processes: (1) segregation of an immiscible Fe-rich silicate melt or Fe-Ti
35 oxide melt from the magma^{5,6}; 2) early crystallization of Fe-Ti oxides with respect to
36 silicates⁷⁻⁹; 3) magma replenishment and mixing¹⁰, or (4) gravity sorting of Fe-Ti
37 oxides^{11,12}. However, all these magmatic models cannot satisfactorily explain the
38 formation of thick massive ores (>60 vol.% Fe-Ti oxides) containing nearly pure
39 monomineralic layers (>90 vol.% Fe-Ti oxides). This is because certain amounts of
40 silicate minerals would inevitably crystallize together with Fe-Ti oxides due to either
41 the presence of Si and Al in the immiscible Fe-rich liquids¹³ or small cotectic
42 proportions of Fe-Ti oxides in the (ferro-) basaltic systems¹⁴.

43

44 Most magmatic rocks in layered intrusions show clear signatures of hydrothermal
45 fluid activities: (1) hydrothermal replacement textures (dissolution/re-precipitation
46 textures)^{15,16}, (2) presence of secondary minerals in or adjacent to the ores¹⁷⁻¹⁹, (3)
47 distinctive core-rim trace element patterns recognized in cumulus minerals^{20,21}, (4)
48 fluid inclusions in minerals²² and (5) stable isotope compositions²³. However, the
49 importance of hydrothermal reworking for the mobilization and concentration of

50 Fe-Ti oxides in layered intrusions is largely overlooked and needs to be elucidated.

51

52 In this study, we combine petrographic observations with *in-situ* elemental- and iron
53 isotope analyses of Fe-Ti oxides from Hongge Fe-Ti oxide deposit to explore the
54 importance of hydrothermal processes in the formation of nearly monomineralic thick
55 massive ore layers. Hongge Fe-Ti deposit is the largest Fe-Ti deposit in Panxi region,
56 southwestern China, and has been invoked as a classical example for magmatic
57 enrichment of Fe-Ti oxides²⁴. However, petrological observations clearly indicate that
58 hydrothermal fluids modified the mineralogy of the magmatic rocks and may be
59 involved in the iron ore formation processes, as evidenced by the presence of hydrous
60 minerals (e.g., chlorite, serpentine, talc, and tremolite)²⁵ in close association with the
61 ores (see Supplementary Figs. 1, 2 for details).

62

63 **Results**

64 **Hongge Fe-Ti deposit and its hosting layered intrusion.** Hongge Fe-Ti deposit is
65 hosted in a sill-like mafic-ultramafic layered intrusion which was emplaced into the
66 Mesoproterozoic marine facies schists and meta-sandstones in the north, and in
67 Neoproterozoic dolomitic limestones and granitic gneisses in the south²⁴. Part of the
68 intrusion at the north-eastern corner is overlain by thick layers of flood basalts²⁵. The
69 northern and western parts of the intrusion are in contact with late Permian alkaline
70 granites and syenites^{26,27} (Supplementary Fig. 1c). Based on the analysis of drill cores,
71 Hongge layered intrusion can be divided into three lithological zones with eleven

72 stratigraphic units (Supplementary Fig. 3), mainly composed of different proportions
73 of olivine, clinopyroxene, plagioclase and Fe-Ti oxides²⁸. The Upper Zone (UZ) is
74 referred to as gabbro zone without any visible ore layers. The Middle Zone (MZ) is
75 composed of four units, which contain magnetite dunite/clinopyroxenite layers on top
76 and Fe-Ti oxide ore layers at the bottom within each unit. Thick massive ore layers
77 (up to ~60m) including monomineralic ore layers occur only at the top of the MZ and
78 are predominantly composed of magnetite and ilmenite. The four units of the Lower
79 Zone (LZ) are mainly dominated by different proportions of coarse-grained cumulus
80 olivine and clinopyroxene while oxides occur as interstitial phases.

81

82 **Textures of silicate and Fe-Ti oxide minerals.** All samples show that alteration
83 textures of primary silicate minerals are widely developed (Supplementary Fig. 3).
84 Primary plagioclase crystals in the UZ are replaced by zoisite. Olivine and
85 clinopyroxene in the MZ and LZ are replaced by serpentine and amphibole. The
86 alteration of olivine to serpentine is particularly strong in the magnetite-bearing dunite
87 layers adjacent to the thick massive ore layers.

88

89 Magnetite and ilmenite were significantly affected by dissolution and/or
90 recrystallization processes. Notably, two generations of magnetite can be
91 distinguished based on compositional and textural characteristics, whereas ilmenite
92 exhibits significant morphological and compositional modifications within a single
93 crystal (Fig. 1). The chemical compositions and occurrence characteristics of both

94 primary and secondary Fe-Ti oxides are also reported in the Supplementary Figs. 4-6
95 and Supplementary Tables 1-4. Particularly, the most important observations can be
96 summarized as follows:

97 (1) Dissolution/alteration textures of magnetites and ilmenites are observed in the
98 samples from Unit I to VI of the LZ to MZ, where the rocks are dominated by
99 silicate layers and there are only two thin ore layers (<5m) with Fe-Ti oxides
100 proportion <60 vol.% (Fig. 1a-d). Magnetite contains abundant exsolution
101 lamella of ilmenite, has jagged edges and is often enclosed by amphibole coronas
102 and cut by amphibole veins (Fig. 1a, b). Ilmenite is partially replaced by titanite
103 or crosscut by titanite veins (Fig. 1c, d).

104 (2) Re-precipitation/recrystallization textures of magnetites and ilmenites are
105 observed in the magnetite-bearing dunite layers (Unit VII, MZ) and in thick
106 massive ore layers (bottom Unit VIII, MZ; Fig. 1e-h). Distinct secondary
107 magnetite is formed as rims surrounding the primary magnetite with a relatively
108 sharp contact (Fig. 1e, f). Chemically, a strong enrichment of secondary
109 magnetite in Fe is accompanied by a strong depletion in Ti, V, Al, Mn and Cr,
110 emphasizing a significant compositional difference between primary and
111 secondary magnetite phases (Supplementary Fig. 5a-f). Ilmenites in Units VII
112 and VIII, MZ display dissolution-recrystallization textures and clear
113 compositional differences or zonation with smooth but large chemical gradients
114 (Fig. 1g, h). The rim compositions of ilmenites are enriched in Fe and depleted in
115 Ti + Mg when compared with the cores (Supplementary Fig. 5g-i). These

116 observations may be related to hydrothermal reworking.

117 (3) The relative proportion of ilmenite over magnetite within ore layers is
118 significantly lower than that in other silicate-rich layers (Fig. 2a; Supplementary
119 Table 5). The massive oxide ores are enriched in magnetite, which may indicate
120 that magnetite is partly of hydrothermal origin, considering that Fe is more
121 effectively mobilized than Ti during hydrothermal ore-forming processes.

122

123 ***In-situ* iron isotopes of primary and secondary Fe-Ti oxides.** The Fe isotopic
124 compositions of Fe-Ti oxides have been systematically investigated using *in-situ*
125 LA-MC-ICP-MS analysis (Supplementary Tables 6, 7). The results show that primary
126 magnetites with dissolution textures, which are observed in Units I and VI (Fig. 1a, b),
127 have relatively high $\delta^{56}\text{Fe}$ values ranging from +0.14 to +0.63‰ (green circles in Fig.
128 2b). In contrast, primary magnetites, surrounded by re-precipitated secondary
129 magnetites that are only observed in Unit VII and at the bottom Unit VIII (Fig. 1e, f),
130 show relatively low $\delta^{56}\text{Fe}$ range (-0.23 to +0.20‰; blue circles in Fig. 2b).
131 Importantly, secondary magnetites in Units VII and VIII have extremely low $\delta^{56}\text{Fe}$
132 values (from -1.24 to -0.09‰; red circles in Fig. 2b) compared to primary magnetites
133 of the same units.

134

135 All ilmenites across the intrusion display low $\delta^{56}\text{Fe}$ values ranging from -1.08 to
136 -0.27‰, with extremely low $\delta^{56}\text{Fe}$ values in Unit VII and at the bottom of Unit VIII
137 (-1.08 to -0.72‰; Fig. 2c). These minima in $\delta^{56}\text{Fe}$ are recorded in ilmenites from the

138 ore layers and closely correspond to the lowest $\delta^{56}\text{Fe}$ values of secondary magnetites.
139 The recrystallized rims or zonation of ilmenite could not be determined because laser
140 beam size was larger than the rims. It is noteworthy that ilmenite displays similar Fe
141 isotope variation patterns to those of primary magnetite throughout the stratigraphic
142 column (except in Lower Zone Unit I; Fig. 2b, c). In other words, both primary
143 magnetite and ilmenite demonstrate coeval evolution of Fe isotopic signatures
144 indicating that isotopic distribution is not controlled by isotopic re-equilibration
145 between coexisting magnetite and ilmenite but rather by an external process such as
146 interaction with hydrothermal fluids.

147

148 **Temperatures recorded by Fe isotope thermometry.** According to our *in-situ* Fe
149 isotope data, most of the primary magnetite-ilmenite pairs plot along with an
150 equilibrium fractionation trend (Fig. 3a). Applying magnetite-ilmenite Fe isotope
151 equilibrium fractionation thermometry^{29,30}, the calculated Fe isotope equilibrium
152 temperatures are in the range of ~300-450°C but most of them plot within an interval
153 of 350 to 450°C (Fig. 3a). In all cases, the resulting temperatures are significantly
154 lower than temperatures that would be expected for isotopic equilibrium at typical
155 magmatic conditions of mafic layered intrusions (1200-950°C^{31,32}; light yellow area
156 in Fig. 3a). Recent studies for Baima intrusion (another layered intrusion in Panxi
157 region) pointed out that the Fe isotope equilibrium temperatures of Fe-Ti oxides could
158 extend to ~650-550°C due to Fe-Ti exchanges (sub-solidus re-equilibration
159 processes³³; light purple area in Fig. 3a). This temperature range is still significantly

160 higher than that observed for Hongge.

161

162 In addition to *in-situ* Fe isotopes, we also determined the Fe-Ti contents of ilmenite
163 and magnetite. Temperatures calculated from the Fe-Ti distribution between primary
164 oxides pairs using QUILF thermometry³⁴ are systematically higher than temperatures
165 calculated from primary magnetite-ilmenite pairs based on Fe isotope fractionation
166 (Fig. 3b). The QUILF temperatures determined in ore layers are higher than that in
167 silicate layers. However, in these ore layers, the Fe-Ti compositions of secondary
168 magnetite and reaction rims of ilmenite pairs provide QUILF temperatures (grey field
169 in Fig. 3b) that are much closer to those obtained from Fe isotope equilibria of
170 primary magnetite and ilmenite. Temperatures from iron isotope distribution between
171 these secondary oxide phases could not be determined because the absence of Fe
172 isotopic compositions of ilmenite rims. The obvious disagreement between Fe
173 isotopic and Fe-Ti compositional equilibrium temperatures for primary phases clearly
174 indicates that a sub-solidus re-equilibration between Fe-Ti oxides during cooling
175 cannot fully explain the isotopic signatures. Thus, an additional process occurring at
176 the temperature of 350-450°C needs to be considered which is likely related to
177 hydrothermal activity. We suggest that observed textural and mineralogical changes
178 and formation of secondary oxides in monomineralic ores from Units VII and VIII are
179 products of interaction between original magmatic rocks and hydrothermal fluids.

180

181 **Discussion**

182 Hydrothermal processes at the late stages of magmatic evolution in layered intrusions
183 can be controlled by the contribution from magmatic fluids exsolved from crystalizing
184 magma as well as by external fluids probably originating from the rocks hosting the
185 intrusion. The latter may be the case for the Hongge intrusion since previous studies
186 indicate that its parental magmas had low water contents²⁵. The wall rocks mainly
187 comprise marine sediments²⁴, potentially containing significant amounts of water with
188 high salinity that may contribute to the formation of hydrothermal fluids around the
189 intrusion. Typically, such hydrothermal fluids are enriched in light Fe isotopes (e.g.
190 $\delta^{56}\text{Fe} = \sim -1.26$ to -0.14 ‰³⁵⁻³⁸). According to experimental data³⁹, iron in
191 hydrothermal Cl-bearing fluids occurs mainly as FeCl_2^0 , which has strong capability of
192 carrying ferrous iron (Fe^{2+}). Although the composition of hydrothermal fluids
193 circulating within Hongge intrusion is still unknown, it can be assumed that they had
194 high salinities and low $\delta^{56}\text{Fe}$ values typical for other hydrothermal fluids. Accordingly,
195 it is likely that some Fe with light Fe isotope composition was added to the Hongge
196 intrusion during a late hydrothermal stage.

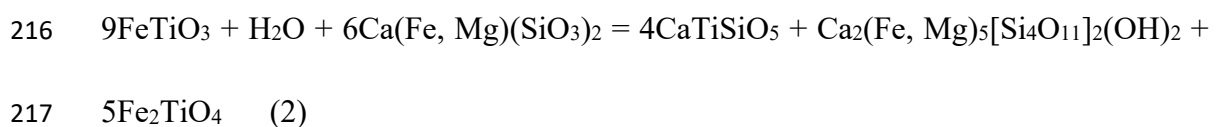
197

198 The petrographic observations presented above clearly indicate that hydrothermal
199 processes played an important role in the reworking of primary magmatic rocks of
200 Hongge intrusion. Magnetite-ilmenite isotopic re-equilibration under hydrothermal
201 conditions can occur through two main mechanisms⁴⁰. The first mechanism is the
202 interaction of magnetite/ilmenite assemblage with a percolating Fe^{2+} -bearing fluid.
203 Application of experimentally determined and calculated isotope fractionation factors

204 (β -factors) for FeCl_2^0 , ilmenite and magnetite^{29,30,41} predict an increase of $\delta^{56}\text{Fe}$ values
205 for magnetite and a decrease of $\delta^{56}\text{Fe}$ values for ilmenite during the hydrothermal
206 re-equilibration process (Supplementary Fig. 8). The second mechanism, which is
207 more commonly invoked, is a hydrothermal dissolution and re-precipitation process
208 because most fluids and especially Cl-rich fluids have strong capabilities for
209 dissolving ferrous Fe (Supplementary Fig. 9). In the Hongge samples, widespread
210 dissolution/alteration textures of primary magnetite and ilmenite in samples of Units I
211 to VI (Fig. 1a-d) suggest that the second mechanism played a dominant role, and a
212 considerable amount of Fe may have been dissolved in and remobilized by fluids
213 according to the simplified magnetite dissolution reaction⁴⁰:



215 and ilmenite alteration reaction⁴²:



218 Magnetite dissolution processes have been discussed in abundant studies and the Fe
219 loss can be estimated with the Rayleigh model^{36,43}. According to the modelling results
220 (Fig. 3c), ~20-30% of primary magnetite in Unit I to VI of the Hongge intrusion may
221 have been dissolved. Compared to Fe, Ti is essentially immobile in the hydrothermal
222 fluids between 300-500°C⁴⁴ (Supplementary Fig. 10a). Hence, it is reasonable to
223 assume that the hydrothermal fluids mainly remobilized Fe, without significant
224 changes in Ti content of the initial rocks. According to the mass balance calculation,
225 the dissolved Fe has the potential to form ~10-16 meter thick ore layers (see Methods

226 below).

227

228 Previous studies showed that Fe solubility in hydrothermal fluids can decrease
229 dramatically during decompression⁴⁵. Thus, further up in the stratigraphic column, the
230 Fe dissolved from the rocks of lower Units could re-precipitate from the hydrothermal
231 fluids, forming secondary magnetite in the ore layers (bottom Unit VIII) and in the
232 adjacent layers (Unit VII). The Fe precipitation process from the hydrothermal fluids
233 was also modelled applying the Rayleigh model and the modelled $\delta^{56}\text{Fe}$ values of
234 secondary magnetite are displayed in Fig. 3d. It is evident that the modelled $\delta^{56}\text{Fe}$
235 results agree with the measured values of secondary magnetite after ca. 20% of
236 precipitation. Since the $\delta^{56}\text{Fe}$ of secondary magnetite is significantly lower than the
237 $\delta^{56}\text{Fe}$ of primary magmatic magnetite (e.g., the ore layers of Baima deposit without
238 hydrothermal reworking in Fig. 3d), re-equilibration between primary and secondary
239 magnetite would easily drive $\delta^{56}\text{Fe}$ of primary magnetite towards lower or even
240 negative values as observed in Unit VII and bottom Unit VIII. In the case of ilmenite,
241 due to the low solubility of Ti in the hydrothermal fluids, no secondary ilmenite was
242 observed in Unit VII and bottom Unit VIII. However, since $\delta^{56}\text{Fe}$ values of primary
243 magnetite are systematically modified towards much lower values, re-equilibrations
244 of magnetite and ilmenite during hydrothermal activity would also shift $\delta^{56}\text{Fe}$ of
245 primary ilmenite towards lower values. There is evidence that Fe-carrying fluids also
246 reacted with primary ilmenite directly through Fe-Mg exchange, forming narrow
247 Fe-rich rims or zonation (Fig. 1g, h) which were, however, unsuitable for accurate Fe

248 isotope analyses. As light Fe isotope diffuse faster than heavy Fe isotopes⁴⁶, Fe-Mg
249 exchange diffusion between primary ilmenite and such Fe-rich rims would further
250 drive Fe isotope compositions of ilmenite towards lighter values. Therefore, we
251 suggest that the low Fe isotope values of primary magnetite and ilmenite in the thick
252 massive ore layers and adjacent layers were generated by isotope re-equilibration in
253 the course of abundant hydrothermal re-precipitation of secondary oxides. Assuming
254 that most of dissolved Fe was re-precipitated from the fluid, this process might be
255 able to enhance both ore tonnages and grades by ~17-27% based on mass balance
256 estimates.

257

258 Based on petrographic observations and Fe isotope compositions of Fe-Ti oxides, we
259 propose a new magmatic-hydrothermal model for the formation of thick massive ores
260 layers in the Hongge intrusion. At the magmatic stage, silicate and Fe-Ti oxide
261 minerals crystallized together as primary silicate-bearing ore layers (<60% Fe-Ti
262 oxides) in the MZ and Fe-Ti oxide-bearing silicate layers (~10-20% Fe-Ti oxides) in
263 the LZ (Fig. 4a). During a hydrothermal stage, the upward flow of fluids could
264 dissolve/alter the igneous minerals and remobilize Fe in both LZ and MZ. The
265 solubility of minerals in hydrothermal fluids typically decreases with decreasing
266 temperature and pressure. However, experimental data and modelling show that the
267 solubility of silicate minerals can be affected by a retrograde dissolution mechanism
268 (Supplementary Fig. 10b), which can increase solubility of SiO₂ by about an order of
269 magnitude in a temperature range of 350-550°C and pressure < 100 MPa⁴⁴. In contrast,

270 the solubility of Fe-Ti oxides remains unaffected by retrograde dissolution reactions⁴⁵
271 (Supplementary Fig. 9). It implies that at the hydrothermal conditions of 350-550°C
272 and shallow pressures in the intrusion, hydrothermal fluids might be able to dissolve
273 and remove part of silicate minerals and precipitate Fe-rich minerals (Fig. 4b). This
274 hydrothermal reworking process could be most efficient at optimal P-T conditions
275 corresponding to the upper MZ layer in the Hongge intrusion resulting in the
276 formation of thick massive or even monomineralic Fe-Ti oxide ore layers. Our model
277 is in accordance with the observed Fe isotopic compositions of minerals through the
278 intrusion (Fig. 4c) and may be applicable to other Fe-Ti oxide deposits with extremely
279 enriched ore layers hosted by layered intrusions.

280

281 So far, the available Fe isotope studies on Fe-Ti oxide ores in layered intrusions were
282 obtained from mineral separates^{33,47,48}. Thus, core/rim variations could not be resolved,
283 in contrast to this study. Nevertheless, various degrees of hydrothermal alteration
284 have also been observed in many other intrusions^{16,17}. Interestingly, the altered
285 layered intrusions always have much wider and higher positive Fe isotope values of
286 magnetite (e.g., ~0.28 to 0.86‰ in the Upper Zone of Bushveld⁴⁸) similar to the
287 observations in Hongge intrusion (Supplementary Fig. 11). These high values may be
288 caused by dissolution processes as described above, resulting in abundant Fe
289 remobilization in the layered intrusions. A similar process of hydrothermal Fe
290 redistribution was also inferred from *in-situ* Fe isotope investigations of magnetite
291 and ilmenite in altered oceanic layered gabbros⁴⁰. Therefore, we propose that

292 hydrothermal reworking could play a key role in the formation of World-class Fe-Ti
293 oxides deposits hosted by layered intrusions.

294

295 **Methods**

296 **Sampling and mineral composition analyses.** Twenty samples from MZ and LZ
297 which are considered to have direct genetic relationships with ore-forming processes
298 were collected for *in-situ* Fe isotope analyses and 34 samples with all the
299 representative Fe-Ti oxides textures are selected for microprobe analyses with an
300 interval at ~20-30 m. Backscatter electron images (BSE) were typically captured
301 under the working condition with 15 kV accelerating voltage and 15 nA beam current
302 through Cameca microprobe.

303 The major and trace elements of magnetite and ilmenite were analyzed with a Cameca
304 SX100 electron microprobe at the Institute of Mineralogy, Leibniz Universität
305 Hannover (Germany). Analytical conditions were set at an accelerating voltage of 15
306 kV and beam current of 100 nA. The beam size was fixed at 5 μm during the whole
307 analysis. The counting times were 10 s on the peak for each element. Standards used
308 for calibrations include quartz (Si), Woll MAC (Ca), chromite (Cr) and synthetic TiO_2 ,
309 Fe_2O_3 , MgO , Al_2O_3 , Mn_3O_4 , V and NiO. PAP procedure was applied for late
310 correction of raw data. The precision for oxide concentrations was better than 1%.

311

312 ***In-situ* Fe isotope determinations by fs-LA-MC-ICP-MS.** A high mass resolution
313 MC-ICP-MS (Thermo Scientific Neptune Plus) connected to a Spectra-Physics

314 Solstice femtosecond laser ablation system was applied to measure Fe isotope
315 compositions at the Institute of Mineralogy, Leibniz Universität Hannover (Germany).
316 The UV femtosecond laser ablation system is based on a 100 femtosecond Ti-sapphire
317 regenerative amplifier system (Hurricane I, Spectra-Physics) and is described in detail
318 by ref.⁵¹. The measurements of Fe isotopes were conducted following the analytical
319 protocol of refs.^{52,53}. Raster-mode was used during mineral analyses and repetition
320 rates varied between 5 and 20 Hz depending on the FeO content of Fe-Ti oxides to
321 keep a relatively constant signal intensity of between 10 and 20 V on mass ⁵⁶Fe. For
322 mass bias correction, a 2 ppm Ni solution was added via a quartz glass spray chamber
323 (double pass Scott design) - which was equipped with an ESI PFA-ST nebulizer and
324 connected with the Laser ablation sample, before introduction into the plasma for
325 simultaneous isotope analyses. Additionally, a sample-standard-bracketing method
326 was applied to correct for the instrumental mass bias drift. Each analysis was
327 performed for a period of 160 s, including 40 s for background analyses (with laser
328 off) and 120 s for sample analyses. The pure Fe-metal IRMM-014 was used as
329 bracketing standard. The raw data were processed with LamTool excel tool. Isotope
330 compositions are reported as $\delta^{56}\text{Fe}$ values relative to IRMM-014 and were determined
331 as follows:

$$332 \quad \delta^{56}\text{Fe} = \left[\frac{\left(\frac{^{56}\text{Fe}}{^{54}\text{Fe}}\right)_{\text{sample}}}{\left(\frac{^{56}\text{Fe}}{^{54}\text{Fe}}\right)_{\text{IRMM-014}}} - 1 \right] \times 1000.$$

333 As no natural standards for magnetite and ilmenite exist, a secondary standard
334 material, JM Puratronic iron standard (99.995%, Puratronic, Johnson Matthey, lot No.
335 FE495007IF2; $\delta^{56}\text{Fe} = 0.09 \pm 0.05\%$ ⁵²) was used to check the performance and

336 stability of the analytical setup. The Fe isotope composition for Puratronic relative to
 337 IRMM-014 well agrees with previously determined values (Supplementary Table 8)
 338 ensuring high precision and accuracy of the *in-situ* Fe isotope analysis conducted in
 339 this study. Several previous studies have shown that all investigated minerals can be
 340 accurately and reliably analyzed with fs-LA-MC-ICP-MS relative to iron metal^{40,52-55}.
 341 All individual samples analyzed in this study, including magnetite, ilmenite, and metal
 342 plot along a mass-dependent fractionation line (Supplementary Fig. 7) which proves
 343 high reliability for the *in-situ* analyses.

344

345 **Equilibrium temperatures calculated in Fig. 3a.** Based on the previous
 346 experimental studies for magnetite and ilmenite^{29,30}, the $\beta^{56}\text{Fe}$ factor (reduced isotopic
 347 partition function ratio) of magnetite and ilmenite were determined as,

$$348 \quad 10^3 \ln \beta_{\text{Mt}}^{56} \approx 0.64394 \times 10^6 / T^2, \text{ and } 10^3 \ln \beta_{\text{Ilm}}^{56} \approx (0.37934/1.5) \times 10^6 / T^2.$$

349 Hence, the possible iron isotope thermometer of magnetite-ilmenite have been
 350 calibrated as,

$$351 \quad 10^3 \ln \beta_{\text{Mt-Ilm}} = 10^3 \ln \beta_{\text{Mt}} - 10^3 \ln \beta_{\text{Ilm}} = \Delta^{56}\text{Fe}_{\text{Mt-Ilm}} = \delta^{56}\text{Fe}_{\text{Mt}} - \delta^{56}\text{Fe}_{\text{Ilm}} \approx [0.64394 -$$

$$352 \quad (0.37934/1.5)] \times 10^6 / T^2 \approx 0.40 \times 10^6 / T^2 \quad (1),$$

353 where T is the absolute temperature in Kelvin.

354

355 **QUILF calculations in Fig. 3b.** Program QUILF³⁴ is a software package that can be
 356 used to assess the equilibrium conditions among Ti-magnetite, ilmenite, augite,
 357 pigeonite, orthopyroxene, olivine and quartz through the QUILF (Quartz - Ulvöspinel

358 - Ilmenite - Fayalite) equilibrium:



360 Depending on the assemblage, various physical-chemical parameters could be
361 estimated (e.g., temperature, pressure, oxygen fugacity, etc). With ilmenite and
362 magnetite pairs in this study, QUILF equilibria could easily provide reliable
363 information of temperature and oxygen fugacity with low uncertainties.

364

365 **Rayleigh fractionation model in Fig. 3c.** The equations that governs magnetite Fe
366 isotope Rayleigh fractionation processes in Fig. 3c are,

$$367 \quad \delta^{56}\text{Fe}_{\text{Mt (hydrothermal dissolution)}} = (1000 + \delta^{56}\text{Fe}_{\text{Mt-primary}}) \times f^{\alpha^{\text{Fluid-Mt}}-1} - 1000 \quad (3)$$

368 where the fractionation factor $\alpha^{\text{Fluid-Mt}}$ is scaled by refs.^{30,41}. Since the primary
369 magnetite in Hongge Fe-Ti deposit has been strongly modified by hydrothermal fluids
370 and has no clue to identify their primary magmatic Fe isotope value, thus the range of
371 $\delta^{56}\text{Fe}_{\text{Mt-primary}}$ is selected from the Fe isotope ranges (0.1 to 0.35‰) in unaltered Baima
372 Fe-Ti deposit³³ in the same region and f represents the fraction of Fe remaining in the
373 primary magnetite. Meanwhile, assuming the hydrothermal fluids were in
374 equilibration with magnetite during the dissolution process, the Fe isotope values of
375 hydrothermal fluids can be scaled by the following equation,

$$376 \quad \delta^{56}\text{Fe}_{\text{Fluids}} = \delta^{56}\text{Fe}_{\text{Mt (hydrothermal dissolution)}} - \Delta^{56}\text{Fe}_{\text{Mt-Fluids}} \quad (4),$$

377 where $\Delta^{56}\text{Fe}_{\text{Mt-Fluids}} \approx 1000\ln(\alpha^{\text{Mt-Fluids}})$.

378 Model lines at 450°C and 350°C describe Rayleigh fractionation process for a
379 fractionation factor $\alpha^{\text{Mt-Fluids}}$ of 1.00042 and 1.00057 or $\alpha^{\text{Fluids-Mt}}$ of 0.99958

380 and 0.99943, respectively.

381

382 **Rayleigh fractionation model in Fig. 3d.** For the re-precipitation process of
383 secondary magnetite in Fig. 3d, the Fe isotope range of hydrothermal fluids obtained
384 from equation (4) during hydrothermal dissolution process is selected as the starting
385 values ($\delta^{56}\text{Fe}_{\text{Fluid-start}} = \sim -0.45$ to 0 ‰). The Fe isotope variations of hydrothermal
386 fluids during Fe re-precipitation process can be calculated according to the Rayleigh
387 equation,

$$388 \quad \delta^{56}\text{Fe}_{\text{Fluid}}^f = (\delta^{56}\text{Fe}_{\text{Fluid-start}} + 1000) \times f^{\alpha^{\text{Mt-Fluid}}-1} - 1000 \quad (5),$$

389 where the fractionation factor $\alpha^{\text{Mt-Fluid}}$ is calculated from refs.^{30,41} and f is the fraction
390 of Fe remaining in the fluids.

391 The “snapshot” $\delta^{56}\text{Fe}_{\text{secondary Mt}}^f$ at a given fraction f can then be determined by
392 Equation (6),

$$393 \quad \delta^{56}\text{Fe}_{\text{secondary Mt}}^f = \delta^{56}\text{Fe}_{\text{Fluid}} + \Delta^{56}\text{Fe}_{\text{Mt-Fluid}} \quad (6)$$

394 where $\Delta^{56}\text{Fe}_{\text{Mt-Fluids}} \approx 1000\ln(\alpha^{\text{Mt-Fluids}})$. The fractionation factor $\alpha^{\text{Mt-Fluids}}$ for
395 modelling at 450°C and 350°C is the same as mentioned in Fig. 3c.

396

397 **Mass balance calculations.** The thickness (Tn) of Unit I to VI is about 350 meters in
398 this studied drill core and proportions (Pr) of magnetite vary from ~6 to 30% (average
399 ~15%, Supplementary Table 5), so the total Fe loss ($T_{\text{Fe-L}}$) during the hydrothermal
400 dissolution process can be obtained from a simple mass balance calculation according
401 to the following equation,

402 $T_{\text{Fe-L}} = T_n \times \text{Pr} \times F$ (7)

403 where F is the fraction of Fe loss calculated from Fig. 3c. The results indicate that the
404 dissolved Fe is an important Fe source and has the potential to form ~10-16 meter
405 thick ore layers.

406 If we considered that the dissolved Fe could all re-precipitate as secondary magnetite
407 into the primary silicate-bearing ore layers, the total thickness of hydrothermally
408 formed layers should correspond to the amount of Fe dissolved in the fluids. The
409 observed thickness of the massive ore layers in the studied drill core are about 60
410 meters in total, so the hydrothermal contributions should be ~10/60 to 16/60 which
411 can also be directly expressed as ~17-27%.

412

413 **Data availability**

414 The authors declare that all relevant data are available within the article and its
415 supplementary information files.

416

417 **References**

- 418 1. Eales, H. V. & Cawthorn, R. G. *Developments in Petrology: The Bushveld complex* (Vol.
419 **15**, 181–229, Elsevier, 1996).
- 420 2. Miller Jr, J. D. & Ripley, E. M. *Developments in Petrology: Layered intrusions of the*
421 *Duluth complex, Minnesota, USA* (Vol. **15**, 257–301, Elsevier, 1996).
- 422 3. Parks, J. & Hill, R. E. T. Phase compositions and cryptic variation in a 2.2-km section of
423 the Windimurra layered gabbroic intrusion, Yilgarn Block, Western Australia; a
424 comparison with the Stillwater Complex. *Econ. Geol.* **81**, 1196–1202 (1986).
- 425 4. Wilson, J. R., Robins, B., Nielsen, F. M., Duchesne, J. C. & Vander Auwera.
426 *Developments in Petrology: The Bjerkreim-Sokndal layered intrusion, Southwest Norway*
427 (Vol. **15**, 231–255, Elsevier, 1996).
- 428 5. Zhou, M. F. et al. Geochemistry, petrogenesis and metallogenesis of the Panzhihua
429 gabbroic layered intrusion and associated Fe-Ti-V oxide deposits, Sichuan Province, SW

- 430 China. *J. Petrol.* **46**, 2253–2280 (2005).
- 431 6. Fischer, L. A. et al. Immiscible iron-and silica-rich liquids in the Upper Zone of the
432 Bushveld Complex. *Earth Planet. Sci. Lett.* **443**, 108–117 (2016).
- 433 7. Pang, K. N., Zhou, M. F., Lindsley, D., Zhao, D. & Malpas, J. Origin of Fe-Ti oxide ores
434 in mafic intrusions: evidence from the Panzhihua intrusion, SW China. *J. Petrol.* **49**,
435 295–313 (2008).
- 436 8. Ganino, C., Arndt, N. T., Zhou, M. F., Gaillard, F. & Chauvel, C. Interaction of magma
437 with sedimentary wall rock and magnetite ore genesis in the Panzhihua mafic intrusion,
438 SW China. *Miner. Depos.* **43**, 677–694 (2008).
- 439 9. Ganino, C., Harris, C., Arndt, N. T., Prevec, S. A. & Howarth, G. H. Assimilation of
440 carbonate country rock by the parent magma of the Panzhihua Fe-Ti-V deposit (SW
441 China): evidence from stable isotopes. *Geosci. Front.* **4**, 547–554 (2013).
- 442 10. Howarth, G. H. & Prevec, S. A. Trace element, PGE, and Sr-Nd isotope geochemistry of
443 the Panzhihua mafic layered intrusion, SW China: Constraints on ore-forming processes
444 and evolution of parent magma at depth in a plumbing-system. *Geochim. Cosmochim.*
445 *Acta* **120**, 459–478 (2013).
- 446 11. Cawthorn, R. G. & Ashwal, L. D. Origin of anorthosite and magnetite layers in the
447 Bushveld Complex, constrained by major element compositions of plagioclase. *J. Petrol.*
448 **50**, 1607–1637 (2009).
- 449 12. Song, X. Y. et al. Formation of thick stratiform Fe-Ti oxide layers in layered intrusion
450 and frequent replenishment of fractionated mafic magma: evidence from the Panzhihua
451 intrusion, SW China. *Geochem. Geophys. Geosy.* **14**, 712–732 (2013).
- 452 13. Wang, M., Veksler, I., Zhang, Z., Hou, T. & Keiding, J. K. The origin of nelsonite
453 constrained by melting experiment and melt inclusions in apatite: The Damiao
454 anorthosite complex, North China Craton. *Gondwana Res.* **42**, 163–176 (2017).
- 455 14. Toplis, M. J. & Carroll, M. R. Differentiation of ferro-basaltic magmas under conditions
456 open and closed to oxygen: implications for the Skaergaard intrusion and other natural
457 systems. *J. Petrol.* **37**, 837–858 (1996).
- 458 15. Arai, S. & Akizawa, N. Precipitation and dissolution of chromite by hydrothermal
459 solutions in the Oman ophiolite: New behavior of Cr and chromite. *Am. Mineral.* **99**,
460 28–34 (2014).
- 461 16. Yudovskaya, M. A. et al. Bushveld symplectic and sieve-textured chromite is a result of
462 coupled dissolution-reprecipitation: a comparison with xenocrystic chromite reactions in
463 arc basalt. *Contrib. Mineral. Petrol.* **174**, 1–21 (2019).
- 464 17. Bindeman, I. N., Brooks, C. K., McBirney, A. R. & Taylor, H. P. The low- $\delta^{18}\text{O}$ late-stage
465 ferrodiorite magmas in the Skaergaard Intrusion: Result of liquid immiscibility, thermal
466 metamorphism, or meteoric water incorporation into magma? *J. Geol.* **116**, 571–586
467 (2008).
- 468 18. Li, H. et al. Alteration of the Damiao anorthosite complex in the northern North China
469 Craton: implications for high-grade iron mineralization. *Ore Geol. Rev.* **57**, 574–588
470 (2014).
- 471 19. Wotzlaw, J. F., Bindeman, I. N., Schaltegger, U., Brooks, C. K. & Naslund, H. R.
472 High-resolution insights into episodes of crystallization, hydrothermal alteration and
473 remelting in the Skaergaard intrusive complex. *Earth Planet. Sci. Lett.* **355**, 199–212

- 474 (2012).
- 475 20. Xing, C. M. & Wang, C. Y. Cathodoluminescence images and trace element
476 compositions of fluorapatite from the Hongge layered intrusion in SW China: A record
477 of prolonged crystallization and overprinted fluid metasomatism. *Am. Mineral.* **102**,
478 1390–1401 (2017).
- 479 21. Zirner, A. L., Marks, M. A., Wenzel, T., Jacob, D. E. & Markl, G. Rare earth elements in
480 apatite as a monitor of magmatic and metasomatic processes: The Ilimaussaq complex,
481 South Greenland. *Lithos* **228**, 12–22 (2015).
- 482 22. Li, L. X. et al. Role of fluids in Fe-Ti-P mineralization of the Proterozoic Damiao
483 anorthosite complex, China: Insights from baddeleyite-zircon relationships in ore and
484 altered anorthosite. *Ore Geol. Rev.* **115**, 103186 (2019).
- 485 23. Schannor, M. et al. Small-scale Sr and O isotope variations through the UG2 in the
486 eastern Bushveld Complex: The role of crustal fluids. *Chem. Geol.* **485**, 100–112 (2018).
- 487 24. Bai, Z. J., Zhong, H., Hu, R. Z. & Zhu, W. G. World-class Fe-Ti-V oxide deposits
488 formed in feeder conduits by removing cotectic silicates. *Econ. Geol.* **116**, 681–691
489 (2021).
- 490 25. Luan, Y. et al. Key factors controlling the accumulation of the Fe-Ti oxides in the
491 Hongge layered intrusion in the Emeishan Large Igneous Province, SW China. *Ore Geol.*
492 *Rev.* **57**, 518–538 (2014).
- 493 26. Shellnutt, J. G. & Jahn, B. M. Formation of the Late Permian Panzhihua
494 plutonic-hypabyssal-volcanic igneous complex: implications for the genesis of Fe-Ti
495 oxide deposits and A-type granites of SW China. *Earth Planet. Sci. Lett.* **289**, 509–519
496 (2010).
- 497 27. Shellnutt, J. G. et al. Three Fe-Ti oxide ore-bearing gabbro-granitoid complexes in the
498 Panxi region of the Permian Emeishan large igneous province, SW China. *Am. J. Sci.*
499 **311**, 773–812 (2011).
- 500 28. Wang, D., Hou, T., Wang, M. & Holtz, F. New constraints on the open magma chamber
501 processes in the formation of giant Hongge Fe-Ti-V oxide deposit. *Lithos* **374**, 105704
502 (2020).
- 503 29. Polyakov, V. B. & Mineev, S. D. The use of Mössbauer spectroscopy in stable isotope
504 geochemistry. *Geochim. Cosmochim. Acta* **64**, 849–865 (2000).
- 505 30. Polyakov, V. B., Clayton, R. N., Horita, J. & Mineev, S. D. Equilibrium iron isotope
506 fractionation factors of minerals: reevaluation from the data of nuclear inelastic resonant
507 X-ray scattering and Mössbauer spectroscopy. *Geochim. Cosmochim. Acta* **71**,
508 3833–3846 (2007).
- 509 31. Johnson, C., Beard, B. & Weyer, S. *Iron Geochemistry: An Isotopic Perspective*. Ch. 4
510 (Springer, Cham, 2020).
- 511 32. Zhang, X. Q. et al. Fractional crystallization and the formation of thick Fe-Ti-V oxide
512 layers in the Baima layered intrusion, SW China. *Ore Geol. Rev.* **49**, 96–108 (2012).
- 513 33. Chen, L. M. et al. Iron isotope fractionation during crystallization and sub-solidus
514 re-equilibration: Constraints from the Baima mafic layered intrusion, SW China. *Chem.*
515 *Geol.* **380**, 97–109 (2014).
- 516 34. Andersen, D. J., Lindsley, D.H. & Davidson, P. M. QUILF: A Pascal program to assess
517 equilibria among Fe-Mg-Mn-Ti oxides, pyroxene, olivine, and quartz. *Comput. Geosci.*

- 518 **19**, 1333–1350 (1993).
- 519 35. Beard, B. L., Johnson, C. M., Von Damm, K. L. & Poulson, R. L. Iron isotope
520 constraints on Fe cycling and mass balance in oxygenated Earth oceans. *Geology* **31**,
521 629–632 (2003).
- 522 36. Rouxel, O., Shanks III, W. C., Bach, W. & Edwards, K. J. Integrated Fe-and S-isotope
523 study of seafloor hydrothermal vents at East Pacific Rise 9-10 N. *Chem. Geol.* **252**,
524 214–227 (2008).
- 525 37. Sharma, M., Polizzotto, M. & Anbar, A. D. Iron isotopes in hot springs along the Juan de
526 Fuca Ridge. *Earth Planet. Sci. Lett.* **194**, 39–51 (2001).
- 527 38. Li, X., Wang, J. & Wang, H. Fe isotopic compositions of modern seafloor hydrothermal
528 systems and their influence factors. *J. Chem.* (2017).
- 529 39. Scholten, L. et al. Solubility and speciation of iron in hydrothermal fluids. *Geochim.*
530 *Cosmochim. Acta* **252**, 126–143 (2019).
- 531 40. Dziony, W. et al. In-situ Fe isotope ratio determination in Fe-Ti oxides and sulfides from
532 drilled gabbros and basalt from the IODP Hole 1256D in the eastern equatorial Pacific.
533 *Chem. Geol.* **363**, 101–113 (2014).
- 534 41. Hill, P. S., Schauble, E. A. & Young, E. Effects of changing solution chemistry on
535 Fe³⁺/Fe²⁺ isotope fractionation in aqueous Fe-Cl solutions. *Geochim. Cosmochim. Acta*
536 **74**, 6669–6689 (2010).
- 537 42. Frost, B. R., Chamberlain, K. R. & Schumacher, K. C. Sphene (titanite): phase relations
538 and role as a geochronometer. *Chem. Geol.* **172**, 131–148 (2001).
- 539 43. Zhu, Z. et al. Iron isotope behaviour during fluid/rock interaction in K-feldspar alteration
540 zone-a model for pyrite in gold deposits from the Jiaodong Peninsula, East China.
541 *Geochim. Cosmochim. Acta* **222**, 94–116 (2018).
- 542 44. Dolejš, D. & Manning, C. E. Thermodynamic model for mineral solubility in aqueous
543 fluids: theory, calibration and application to model fluid-flow systems. *Geofluids* **10**,
544 20–40 (2010).
- 545 45. Simon, A. C., Pettke, T., Candela, P. A., Piccoli, P. M. & Heinrich, C. A. Magnetite
546 solubility and iron transport in magmatic-hydrothermal environments. *Geochim.*
547 *Cosmochim. Acta* **68**, 4905–4914 (2004).
- 548 46. Oeser, M., Dohmen, R., Horn, I., Schuth, S. & Weyer, S. Processes and time scales of
549 magmatic evolution as revealed by Fe-Mg chemical and isotopic zoning in natural
550 olivines. *Geochim. Cosmochim. Acta* **154**, 130–150 (2015).
- 551 47. Cao, Y., Wang, C. Y., Huang, F. & Zhang, Z. Iron isotope systematics of the Panzhihua
552 mafic layered intrusion associated with giant Fe-Ti oxide deposit in the Emeishan large
553 igneous province, SW China. *J. Geophys. Res. - Sol. Ea.* **124**, 358–375 (2019).
- 554 48. Bilenker, L. D., VanTongeren, J. A., Lundstrom, C. C. & Simon, A. C. Iron isotopic
555 evolution during fractional crystallization of the uppermost Bushveld Complex layered
556 mafic intrusion. *Geochem. Geophys. Geosy.* **18**, 956–972 (2017).
- 557 49. Troll, V. R. et al. Global Fe-O isotope correlation reveals magmatic origin of Kiruna-type
558 apatite-iron-oxide ores. *Nat. Commun.* **10**, 1–12 (2019).
- 559 50. Liu, P. P., Zhou, M. F., Luais, B., Cividini, D. & Rollion-Bard, C. Disequilibrium iron
560 isotopic fractionation during the high-temperature magmatic differentiation of the Baima
561 Fe-Ti oxide-bearing mafic intrusion, SW China. *Earth Planet. Sci. Lett.* **399**, 21–29

- 562 (2014)
- 563 51. Horn, I. & von Blanckenburg, F. Investigation on elemental and isotopic fractionation
564 during 196 nm femtosecond laser ablation multiple collector inductively coupled plasma
565 mass spectrometry. *Spectrochim. Acta B* **62**, 410-422 (2007).
- 566 52. Horn, I., von Blanckenburg, F., Schoenberg, R., Steinhoefel, G. & Markl, G. In situ iron
567 isotope ratio determination using UV-femtosecond laser ablation with application to
568 hydrothermal ore formation processes. *Geochim. Cosmochim. Acta* **70**, 3677-3688
569 (2006).
- 570 53. Oeser, M., Weyer, S., Horn, I. & Schuth, S. High-precision Fe and Mg isotope ratios of
571 silicate reference glasses determined in situ by femtosecond LA-MC-ICP-MS and by
572 solution nebulisation MC-ICP-MS. *Geostand. Geoanal. Res.* **38**, 311-328 (2014).
- 573 54. Steinhoefel, G., Horn, I. & von Blanckenburg, F. Micro-scale tracing of Fe and Si
574 isotope signatures in banded iron formation using femtosecond laser ablation. *Geochim.
575 Cosmochim. Acta* **73**, 5343-5360 (2009).
- 576 55. Günther, T., Klemd, R., Zhang, X., Horn, I. & Weyer, S. In-situ trace element and
577 Fe-isotope studies on magnetite of the volcanic-hosted Zhibo and Chagangnuoer iron ore
578 deposits in the Western Tianshan, NW China. *Chem. Geol.* **453**, 111-127 (2017).

579

580 **Acknowledgements**

581 D.W. and T.H. acknowledge support from Nature Foundation of Sciences in China
582 (41922012 and 41761134086), China Scholarship Council (201706400078) and
583 Alexander von Humboldt Fellowship (1207058). T.H. also acknowledges the
584 Fundamental Research Funds for the Central Universities (265QZ201901),
585 MSFGPMR201804 and B18048. F.H. acknowledge support from the German Science
586 Foundation (DFG, HO1337/39-1).

587

588 **Author contributions**

589 T.H and S.W planned the project. D.W, S.H, T.H, F.H, Z.Z and R.B led field and
590 analytical efforts. D.W. and I.H. produced the new data, compiled and modelled the
591 Fe isotope data. All authors contributed to write the manuscript.

592

593 **Competing interests**

594 The authors declare no competing interests.

595

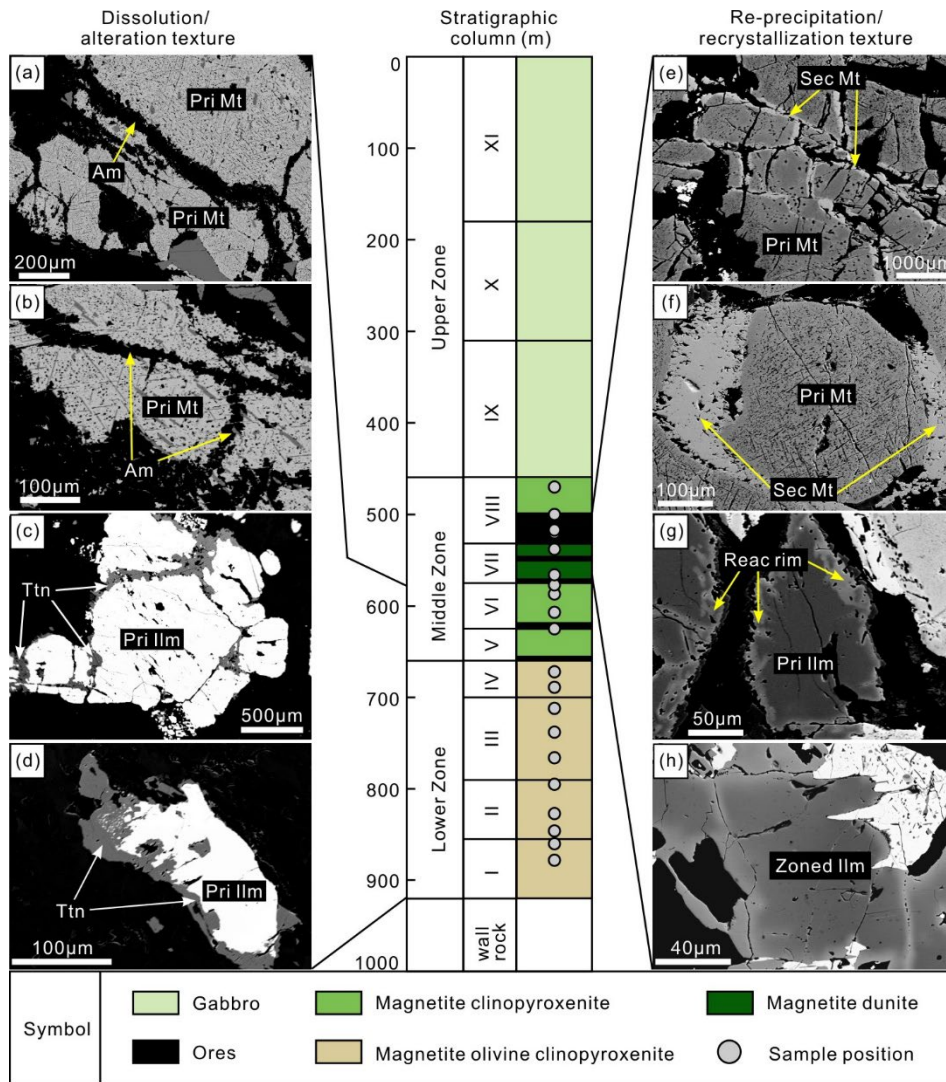
596 **Additional information**

597 Supplementary information is available in the online version of the paper. Reprints
598 and permissions information is available online at www.nature.com/reprints.

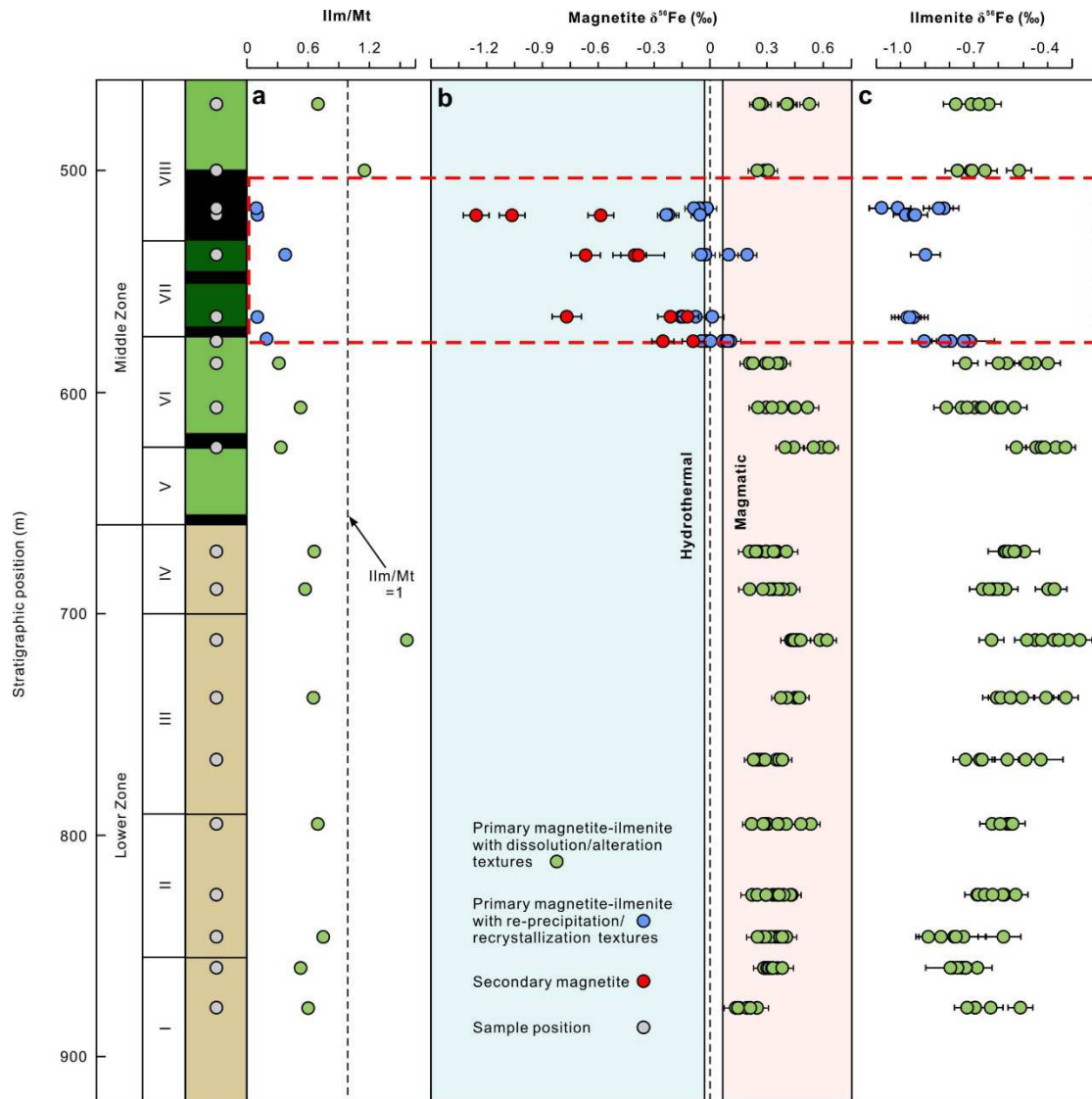
599 Correspondence and requests for materials should be addressed to T.H.

600

601 **Figures and legends**



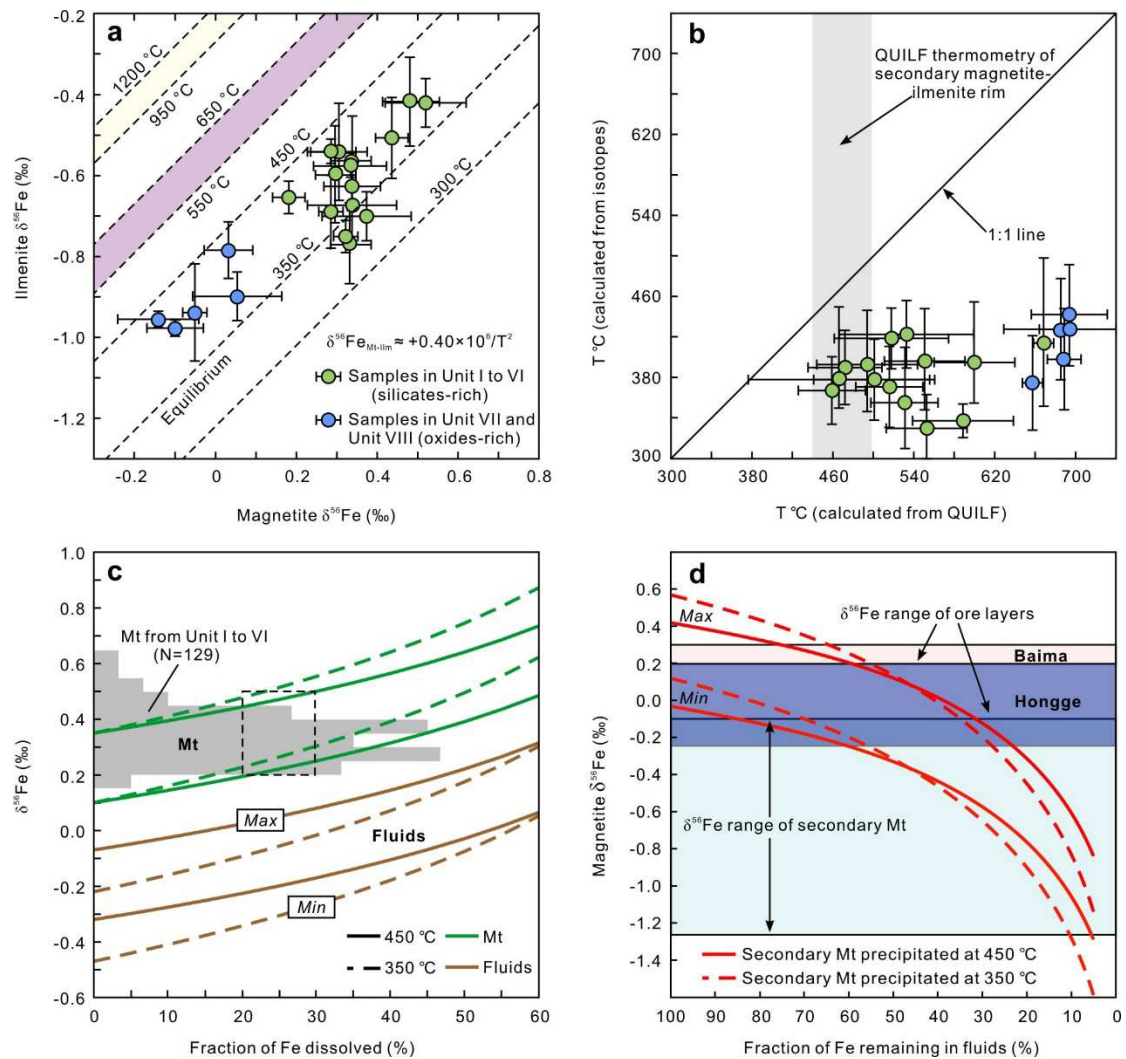
602
 603 **Fig. 1 | Fe-Ti oxides dissolution/alteration textures in Unit I to VI and**
 604 **re-precipitation/recrystallization textures in Unit VII and bottom Unit VIII. a-d** The primary
 605 primary magnetite and ilmenite are either cut or rimmed by hydrothermal replacement, i.e., secondary
 606 amphibole and titanite, respectively. **e-f** Secondary magnetite crystallized as overgrowth rim
 607 surrounded the primary magnetite. **g** Recrystallization of reaction rim in primary ilmenite. **h**
 608 Zonation in the primary ilmenite. Abbreviations: Pri Mt=Primary magnetite; Pri Ilm=Primary
 609 ilmenite; Am=Amphibole; Ttn=Titanite; Sec Mt=Secondary magnetite; Reac rim=Reaction rim;
 610 Zoned Ilm=Zoned ilmenite.
 611



613

614 **Fig. 2 | Ratio of ilmenite/magnetite modal proportions in the samples (a) and *in-situ* Fe**615 **isotope variations for magnetite (b) and ilmenite (c) along the stratigraphic column (data are**616 **from Supplementary Tables 5-7). Each circle represents one individual analyzed spot and each**617 **bar represents the range of $\delta^{56}\text{Fe}$ in one spot including 2σ errors. The red dashed rectangle marks**618 **the sample range of magnetite dunite and thick massive ores. The Fe isotope ranges characteristic**619 **for magmatic (light pink area can extend to $\sim 0.9\%$) and hydrothermal (light blue area) magnetite**620 **ores are from ref.⁴⁹. Symbols for different lithological units in stratigraphic column as per Fig. 1.**621 **Abbreviations: Mt=magnetite, Ilm=ilmenite.**

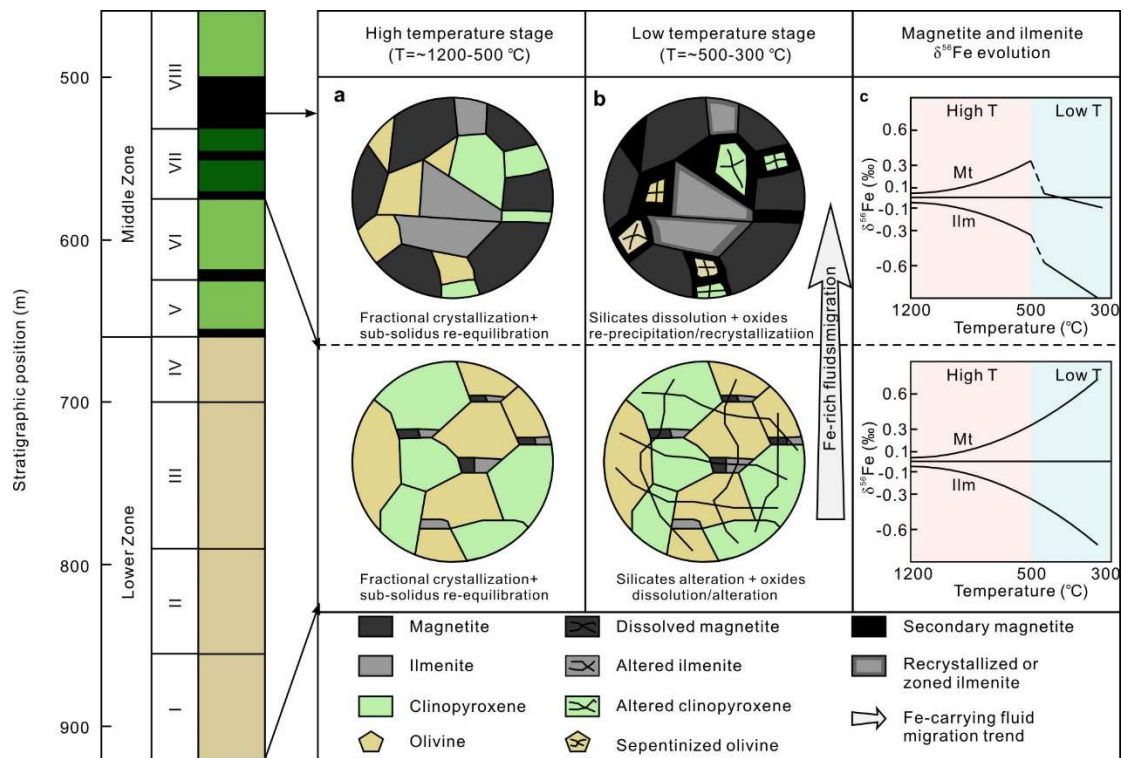
622



624

625 **Fig. 3 | Temperatures constrained from isotopic and elemental thermometry and modelling**
 626 **calculations for hydrothermal dissolution and re-precipitation processes.** **a** Fe isotope
 627 compositions and isotope fractionation isotherms (dashed lines) for primary magnetite and
 628 ilmenite pairs from Hongge Fe-Ti deposit. The light yellow region indicates expected Fe isotope
 629 equilibrium fractionation at magmatic temperatures (1200-950°C³²). The light purple area
 630 represents the range of sub-solidus re-equilibrium temperatures (650-550°C³³). Each circle
 631 represents the average value of analysis within the single thin section (see Supplementary Table 6).
 632 **b** Comparison of primary magnetite-ilmenite equilibrium temperatures between QUILF
 633 thermometry and Fe isotope thermometry (Supplementary Tables 5, 6). The grey field represents
 634 elemental equilibrium temperatures according to secondary magnetite-ilmenite reaction rims
 635 through QUILF thermometry in thick massive ores (bottom Unit VIII) and heavily altered
 636 magnetite dunite layers (Unit VII). **c** Modelled Fe isotope variations for primary magnetite during
 637 hydrothermal dissolution process. The histogram of $\delta^{56}\text{Fe}$ for primary magnetite from Unit I to VI
 638 are provided along the vertical axis to show the main Fe isotope variation range (Data is from
 639 Supplementary Table 6). The solid and dashed lines are illustrated for modelling results at 450°C
 640 and 350°C, respectively. The green color represents magnetite Fe isotope variations during Fe
 641 dissolution process while the brown is used for potential Fe isotope values of hydrothermal fluids

642 which are assumed to be in equilibrium with magnetite during the dissolution process. The dashed
643 box scales for the possible fraction of Fe loss during the dissolution process. **d** Modelled Fe
644 isotope values for secondary magnetite during Fe re-precipitation process. The bottom light blue
645 area represents the $\delta^{56}\text{Fe}$ range of secondary magnetite analyzed in this study (Data is from
646 Supplementary Table 7). The upper light pink area represents the $\delta^{56}\text{Fe}$ range of unaltered
647 magmatic magnetite from ore layer samples in Baima Fe-Ti deposit⁵⁰. The middle dark blue area
648 represents the $\delta^{56}\text{Fe}$ range of primary magnetite from thick massive ores (bottom Unit VIII) and
649 adjacent heavily altered magnetite dunite layers (Unit VII) in the Hongge Fe-Ti deposit.
650 Abbreviation: Mt=magnetite.



652

653 **Fig. 4 | Conceptual model of hydrothermal reworking illustrates the formation processes of**
 654 **thick massive ores. a** Formation of primary silicates-bearing ore layers (upper) and their hosting
 655 silicates layers (lower) in layered intrusions at magmatic and sub-solidus temperatures
 656 (1200-500°C). Under this condition, the ore layers are mainly disseminated with relatively low
 657 oxides proportion of only ~50-60%. **b** Through hydrothermal reworking under low temperatures
 658 (500-300°C), abundant Fe in the silicate layers (lower) could be dissolved and carried upwards by
 659 the hydrothermal fluids. Due to cooling and decompression effects, the dissolved Fe could
 660 re-precipitate into the primary silicates-bearing ore layers (upper). Simultaneously, the silicate
 661 minerals in the primary ore layers where Fe is re-precipitating could be dissolved as a result of
 662 retrograde dissolution of silica in hydrothermal fluids at 500-300°C and P<100 MPa). Eventually,
 663 the primary disseminated ore layers could be “upgraded” into massive ore layers or even
 664 monomineralic ore layers. **c** The Fe isotope evolution during different stages, i.e., primary
 665 magnetite-ilmenite in the hosting silicates layers (lower) and thick massive ore layers (upper) from
 666 magmatic to hydrothermal stage. The dashed part of the lines represent the discontinuous sharp
 667 decrease of the Fe isotopes of primary magnetite and ilmenite in thick massive ore layers due to
 668 hydrothermal precipitation of secondary magnetite. Symbols for different lithological units in
 669 stratigraphic column as per Fig. 1. Abbreviations: Mt=magnetite, Ilm=ilmenite.

670

Supplementary Files

This is a list of supplementary files associated with this preprint. Click to download.

- [SupplementaryData1.xlsx](#)
- [SupplementaryInformation.docx](#)